Improved Power Factor and Mechanical Properties of Composites of $Yb_{14}MgSb_{11}$ with Iron

Christopher J. Perez,[1] Xiao Qi,[1] Zhijie Chen,[2,3] Sabah K. Bux,[4*] Sevan Chanakain,[4] Billy Li,[4] Kai Liu,[2,3] Rohan Dhall,[5] Karen C. Bustillo,[5] and Susan M. Kauzlarich[1*]

[1] Department of Chemistry, University of California, One Shields Ave., Davis, CA 95616, USA.
[2] Department of Physics, University of California, One Shields Ave., Davis, CA 95616, USA.
[3] Physics Department, Georgetown University, Washington, DC 20057, USA.
[4] Thermal Energy Conversion Research and Advancement Group, Jet Propulsion Laboratory, California Institute of Technology, 4800 Oak Grove Drive, Pasadena, CA 91109-8099, USA.
[5] National Center for Electron Microscopy, Molecular Foundry, Lawrence Berkeley National Laboratory, Berkeley, CA 94720, USA.

Keywords: Composite, Thermoelectric, Transport properties, Zintl phase, SPS synthesis, First-order reversal curves.

* Corresponding authors: smkauzlarich@ucdavis.edu; sabah.k.bux@jpl.nasa.gov

Abstract

Composite phases have been shown to improve both the thermoelectric efficiency and mechanical properties of materials. Here we demonstrate an improved thermoelectric figure of merit, power factor, and mechanical properties for the high-temperature *p*-type Zintl phase $Yb_{14}MgSb_{11}$. Composites with 0, 1, 2, 3, 4, 6, 8 volume % 6 – 10 μm reduced Fe powder were prepared via a fast, scalable mechanical milling and spark plasma sintering procedure. Powder X-ray diffraction, scanning electron microscopy, and transmission electron microscopy show that Fe is not incorporated into the $Yb_{14}MgSb_{11}$ structure. First order reversal curves and scanning electron microscopy images show that the Fe inclusions are larger and closer together with increasing Fe content. Thermogravimetric and differential scanning calorimetry show that the composites are stable up to 1273 K. The elastic constants of the 8 volume % Fe composite were measured by resonant ultrasound spectroscopy and show that $Yb_{14}MgSb_{11}$ becomes stiffer with increasing Fe volume % and SEM after indentations show crack arresting occurs at the Fe interface. Thermoelectric properties on dense pellets are measured from 300 K – 1273 K. The thermoelectric power factor ($PF = \frac{S^2}{\rho}$) increases with increasing Fe content, with the 8 volume % Fe resulting in 40% higher PF than pristine $Yb_{14}MgSb_{11}$. The increase in PF is attributed to a systematic reduction in electrical resistivity. Peak thermoelectric figure of merit ($zT = \frac{S^2T}{\kappa\rho}$) is observed at 3 volume % Fe, an 11% improvement in zT compared to $Yb_{14}MgSb_{11}$. $Yb_{14}MgSb_{11}$

composites with Fe are compatible with $Ce_{0.9}Fe_{3.5}Co_{0.5}Sb_{12}$ for thermoelectric generator couple segmentation.

1. Introduction

Thermoelectric generators provide a way to transform heat directly into electricity through the Seebeck effect and have provided power for NASA's deep space exploration missions for decades with high reliability. Current Radioisotope Thermal Generators (RTG) convert at most 7.5% of the heat available to electricity.[1] Providing materials that can more efficiently convert heat to electricity will improve the efficiency of RTGs for future deep space missions and can also be used to recover waste heat on earth. The efficiency of a thermoelectric material is described by the dimensionless thermoelectric figure of merit *zT*. *zT* is defined by a material's Seebeck coefficient *S* (V/K), absolute temperature *T* (K), electrical resistivity ρ (Ω-m), and thermal conductivity κ (W/mK) ($zT = \frac{S^2 T}{\kappa \rho}$).[2]

Efforts to improve zT in existing materials can be divided into two main themes: maximizing power factor ($PF = \frac{S^2}{\rho}$) by band structure engineering such as band convergence, tuning the electronic states with resonance levels, or simple substitutional alloying. There has also been significant research focused around reducing lattice thermal (κ_l) conductivity by nano-structuring, alloy scattering, compositing, or rattler atoms.[3-4] Thermal conductivity ($\kappa_{tot} = \kappa_l + \kappa_e$) consists of an electronic portion (κ_e) and a lattice portion (κ_l). κ_e is coupled to the Seebeck coefficient and electrical resistivity by carrier concentration; however, κ_l is not, and thereby provides a method for increasing zT without affecting the other thermoelectric properties.[5]

Composites can show improvement in thermoelectric properties of a phase by enhanced scattering of mid-long wavelength phonons at the material interfaces with little influence on short wavelength electrons leading to a lower κ_l without increasing ρ.[3, 6-7] Composites have been used to increase the PF of PbTe/$Pb_{1-x}Eu_x$ by modulation doping where charge carriers are spatially separated from their parent impurity atoms to reduce the influence of impurity scattering and thereby increase the mobility of the charge carriers.[8] Recent work on the high temperature *n*-type thermoelectric $La_{3-x}Te_4$ phase has shown that compositing with 15 volume % nickel can result in a zT improvement from 1.1 to 1.9.[9]

In addition to a high zT, thermoelectric materials must have robust mechanical properties to withstand significant mechanical stress during thermal cycling and operation in devices.[10] There have been efforts to composite skutterudites with oxides, metals, antimonides, borides, tellurides, nitrides, and silicides with varying degrees of success in terms of thermoelectric performance; however, in most cases the mechanical properties of the composites improve.[6-7, 11] Improving the mechanical robustness helps the manufacturing of the material and prolongs the thermoelectric device's lifetime.[7, 12] Devices are comprised of *n*-type and *p*-type semiconductors thermally in parallel and electrically in series and are essentially Carnot engines. Their efficiency is defined by $(\eta = \frac{\Delta T}{T_h}\frac{\sqrt{1+ZT}-1}{\sqrt{1+ZT}+\frac{T_h}{T_c}})$[1] where ΔT is the difference between T_h (hot side) and T_c (cold side) and ZT is the average zT over the entire temperature range for both *n*- and *p*-type materials. Peak zT occurs at distinct temperatures for different materials, so a large temperature difference leads to a higher Carnot efficiency. However, if a high zT material gives a low average ZT, the device will have an overall low efficiency. In 2010, the Advance ThermoElectric Converter (ATEC) program at NASA's Jet Propulsion Laboratory (JPL) demonstrated that they could segment a device that coupled (Ba, Yb)$CoSb_3$ and $La_{3-x}Te_4$ on the *n*-type leg and $Ce_{0.9}Fe_{3.5}Co_{0.5}Sb_{12}$ and $Yb_{14}MnSb_{11}$ on the *p*-type leg in order to maximize the ZT and yield efficiencies of 15%.[1] The key for segmenting is to have materials with compatible *S*, ρ, and κ to avoid a large difference in current density. The thermoelectric compatibility factor (α) defined as $\left(\alpha = \frac{\sqrt{1+zT}-1}{ST}\right)$ takes the thermoelectric factors into account. Compatible materials must have an α within a factor of 2 V^{-1} at the junction to avoid efficiency losses due to a mismatch in current density.[13-14]

Some of the highest zT bulk *p*-type thermoelectric materials in the 1000 – 1273 K range are $Yb_{14}MnSb_{11}$ and $Yb_{14}MgSb_{11}$ with a zT of 1.33 at 1273 K and 1.02 at 1073 K, respectively.[15-16] $Yb_{14}MgSb_{11}$ has the $Ca_{14}AlSb_{11}$ structure type (Fig. 1).[16] The large and complex $I4_1/acd$ (6145(8) $Å^3$) unit cell leads to an inherently low thermal conductivity making this structure type ideal for thermoelectric applications.[15] The chemically flexible structure type can be described generally as $A_{14}MPn_{11}$ and can accommodate a variety of alkali and rare earth metals in the A site, a variety of transition metals and Mg in the M site, and the group 15 elements heavier than nitrogen in the Pn site.[15,17] The formula of $Yb_{14}MgSb_{11}$ is close to a charge balanced Zintl phase and can be considered to be comprised of thirteen Yb,$^{2+}$ cations one Yb^{3+} cation, one $[MgSb_4]^{10-}$ tetrahedra, and one $[Sb_3]^{-7}$ linear anion, and four isolated $[Sb]^{-3}$ anions.[15]

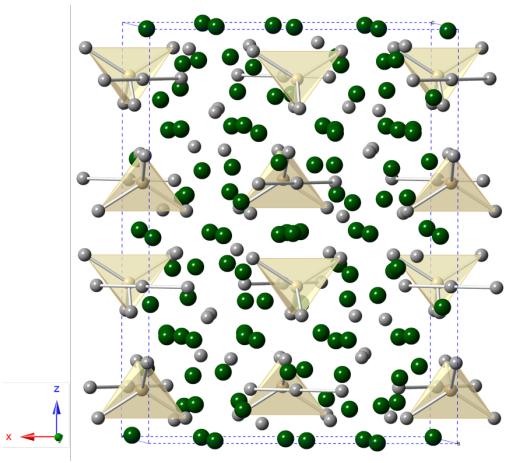

Figure 1. A view along the *b*-axis of the unit cell of $Yb_{14}MgSb_{11}$. The polyhedra of $MgSb_4$ are highlighted. Yb is shown in green, Sb in grey, and Mg in beige.

This work focuses on improving the thermoelectric properties and the mechanical robustness of $Yb_{14}MgSb_{11}$ by means of compositing with *x* volume % of Fe (*x* = 0, 1, 2, 3, 4, 6, 8).[2, 9-10] Micron-sized Fe powder was chosen as the inclusion for compositing because Fe is a *p*-type metal, has a similar coefficient of thermal expansion as $Yb_{14}MgSb_{11}$, and was expected to be an inert additive.[18-19] Additionally, only1/26 atoms in the $Yb_{14}MSb_{11}$ structure type are 'M', making it difficult to produce phase pure powder for consolidation. Researchers ensure the distribution of the 'M' element by using precursors such as MnSb and MgH_2 in excess or large excess of 'M' (100% Zn excess) to avoid the formation of $Yb_{11}Sb_{10}$ and other 'M' deficient side phases.[15, 20-23] In this example, the addition of Fe enhances the ease of synthesis. Fe is known to act as a dry milling aid, potentially coating the milling container and leading to less agglomeration of elements, better powder fluidity, and better elemental dispersion resulting in high reproducibility of the $Yb_{14}MgSb_{11}$ product.[24]

Polycrystalline $A_{14}MPn_{11}$ samples are typically synthesized by stochiometric amounts of the elements A:M:Pn placed in welded Ta or Nb ampoules which are sealed in fused silica under vacuum and annealed at high temperatures (900 °C – 1100 °C) for 4 days in a box furnace; the samples are then consolidated by SPS.[15, 22, 25] The reaction described herein provides a faster approach where samples are mechanically milled and reacted via spark plasma sintering in under 2 hours.

Powder X-ray diffraction (PXRD), scanning electron microscopy (SEM), electron microprobe analysis (EMPA), transmission electron microscopy (TEM), and first order reversal curves (FORC) were performed to investigate the $Yb_{14}MgSb_{11}$ + Fe composite structure. High

temperature (323 - 1273 K) thermoelectric properties of the Fe containing $Yb_{14}MgSb_{11}$ composites were measured. Preliminary mechanical properties such as elastic constants and crack arresting were studied with resonant ultrasound spectroscopy (RUS) and by qualitatively comparing crack patterns.

2. Experimental

2.1 *Materials:* All materials were handled in an argon filled glove box with < 0.1 ppm of oxygen. Mg turnings of 100 mg average mass and Yb turnings of 200 mg average mass from large ingots of Mg (99.9%, MagCan) and Yb (99.95%, Edge Tech). Sb shot (99.999%, 5N Plus) and Fe powder (spherical, APS 6-10 μm, pre-reduced, 99.5%, Alfa Aesar) were used as received.

Mg_3Sb_2 was prepared according to the following procedure adapted from literature:[26] a 10g batch of Mg turnings and Sb shot in a 3:2 molar ratio was placed in an air-tight SPEX tungsten carbide grinding vial set (55 mL, 2 ¼ in. Diameter x 2 ½ in. long) with three ~10.75 g tungsten carbide balls and custom-made Viton® O-rings and milled in a SPEX 8000D mixer/mill. Initially, only one-third of the total Mg is added. After the first hour of milling, all the material is scraped out of the vial with a chisel and then reinserted with an additional 1/3 of Mg and milled for an additional hour. The same procedure is repeated for the third aliquot of Mg. After the third hour of milling the material is scraped out of the vial, reinserted, and milled for an additional 6 hours in 1-hour intervals with 1-hour rest between millings. Sample purity was confirmed by PXRD shown in supporting information (SI) Figure S1.

Caution: Finely milled metals are reactive to moisture and oxygen and should be handled in an inert atmosphere.

2.2 *$Yb_{14}MgSb_{11}$ + x volume % Fe (x = 0, 1, 2, 3, 4, 6, 8):* Synthetic methods were modified from those reported for $Yb_{14}MnSb_{11}$.[22] A 20 g batch of Yb turnings, Sb shot, and Mg_3Sb_2 were placed in a SPEX tungsten carbide grinding vial set described above with two ~10.75 g tungsten carbide balls in a 14.1: 0.4: 10.2 molar ratio and milled for three hours. After every hour of milling, the material was scraped out and re-inserted to ensure that the reagents were evenly dispersed. Three 20 g batches of milled Yb, Mg_3Sb_2, and Sb powders were combined and mixed together using a spatula. Iron was added by combining *x* g (calculated for volume %) Fe powder with (3.5 - *x*) g of the milled Yb, Mg_3Sb_2, Sb powder in an air-tight SPEX tungsten carbide grinding vial set with one ~10.75 g tungsten carbide ball. The mixture was mechanically milled

for 30 min. The resulting powder was scraped out of the vial and 3.0 g of material was placed into a 12.7 mm graphite die with graphite plungers and graphite foils. The die was placed in a spark plasma sintering (Thermal Technology LLC, SPS) reactor and heated under dynamic vacuum to 1200 °C over 48 min and held at temperature for 40 min. 80 MPa of pressure on the cross section was applied over 10 min and retained during the entire heating profile. The products were dark grey metallic disks of ≥ 98% of theoretical density. Sample purity was confirmed by PXRD. The Yb amount resulting in optimal sample purity was investigated by varying the stoichiometry $Yb_{14.x}Mg_{1.2}Sb_{11}$ (x = -0.3, -0.1, 0, 0.1, 0.3), and the composition $Yb_{14.1}Mg_{1.2}Sb_{11}$ was determined to give the samples with the highest purity. Yb excess was needed to compensate for experimentally observed losses of Yb to the grinding vial (SI, Fig. S2). The need for 0.067 excess Mg_3Sb_2 was experimentally determined necessary to obtain the highest $Yb_{14}MgSb_{11}$ purity; presumably, some Mg was vaporized during high temperature reaction under vacuum.

Synthesis of $Yb_{14}FeSb_{11}$ was attempted with the stoichiometric amounts of the elements according to the ball milling and SPS procedure outlined above without the second 30 min milling step.

2.3 *PXRD:* PXRD patterns were collected on a Bruker D8 Eco Advance diffractometer operated at 40 kV and 25 mA at room temperature using Cu radiation from 20° - 90° 2θ with a step size of 0.019°. About 2 wt. % Si was added as an internal standard to calibrate the lattice parameter measurements. Rietveld refinement was performed with the JANA 2006 software package.[27] The crystallographic information files for $Yb_{14}MgSb_{11}$, $Yb_{11}Sb_{10}$, Yb_2O_3, and Fe were used to generate the models for Rietveld refinement. A 30-point manual background, sample height correction, and lattice parameters were fit first. The profile shape was generated with a pseudo-Voigt function. PXRD plots containing Rietveld refinement are shown in SI, Figure S3.

2.4 *SEM:* SEM was obtained with a Scios Dual beam SEM/FIB microscope. Secondary electron imaging was performed using an Everhard-Thornley Detector. Energy dispersive X-ray spectroscopy (EDS) was done with a window-less Oxford instruments X-max 50 equipped with a 50 mm^2 silicon drift detector. Samples of sintered pellets were mounted in epoxy and ground metallographically to a 0.1 μm finish with an oil-based polishing media then carbon coated and placed on aluminum stubs for imaging. ImageJ software was used to qualitatively determine the

area % Fe present and the size of the Fe inclusions.[28]

2.5 *EMPA:* Elemental analysis was performed on sintered pellets of $Yb_{14}MgSb_{11}$ + *x* volume % Fe composites prepared as in Section 2.5 using a Cameca SX-100 electron microprobe equipped with five wavelength-dispersive spectrometers. X-ray maps were collected on *x* = 1, 4 volume % Fe samples. A $Yb_{14}MgSb_{11}$ single crystal was used as the Yb $L\alpha_1$, Mg $K\alpha_1$, and Sb $L\alpha_1$ standard. Hematite was used as the Fe $K\alpha_1$ standard. $Yb_{14}MgSb_{11}$ compositions were averaged from 8 data points and atomic percent was multiplied by 0.26 to give the $Yb_{14}MgSb_{11}$ stoichiometry.

2.6 *FORC:* Magnetic properties were studied by magnetometry and the FORC method[29-32] at room temperature using a Princeton Measurements vibrating sample magnetometer (VSM). For the FORC measurements, the sample was first saturated in a positive magnetic field; then, the magnetic field (H) was decreased to a given reversal field (H_R) and the magnetization was measured while the field was swept back to positive saturation. This process was repeated many times at different H_R, creating a family of FORCs. The FORC distribution can then be calculated using the mixed second-order derivative of the magnetization,[29-32]

$$\rho\,(H, H_R) \equiv -\frac{1}{2M_S}\frac{\partial^2 M(H, H_R)}{\partial H\,\partial H_R},$$

where M_S is the saturation magnetization, and $M(H, H_R)$ is the magnetization at the applied field H with reversal field H_R. It is also sometimes convenient to change the coordinates from (H, H_R) to (H_C, H_B) through a transformation defined by[32-34]

$$H_B = \frac{1}{2}(H + H_R), H_C = \frac{1}{2}(H - H_R),$$

where H_C is the local coercive field and H_B is the bias field.

2.7 *TEM*: TEM samples were prepared by mechanical polishing on diamond lapping films followed by Ar-ion milling at 5 keV then 2.5 keV with 3° angle of incidence to electron transparency. TEM data were acquired using a FEI ThemIS 60 - 300 STEM/TEM (Thermo Fisher Scientific, US) operated at 300 kV at the National Center for Electron Microscopy within the Molecular Foundry in Lawrence Berkeley National Laboratory. The ThemIS is equipped with image aberration corrector optics, and a Ceta2 camera (4kx4k pixels, and 14-bit dynamic range). EDS was performed using a Bruker Super-X Quad windowless detector with a solid angle of 0.7 steradian.

2.8 *Vickers Hardness:* Hardness measurements were done as outlined in literature.[35-36]

$Yb_{14}MgSb_{11}$+ x volume % Fe (x = 0, 8) consolidated pelleted samples typically 12.7 mm diameter and 1.5 mm thick were polished parallel and flat to ±0.05 mm. Samples were ground metallographically to a 0.01 μm finish with an oil based polishing media. Vickers indentation hardness measurements were done with a Wilson Hardness Tukon T2100B instrument with a maximum 1000 gf load cell. Spalling was seen after 500 gf so only data up to 500 gf was reported (SI, Fig. S4, S5). Practices outlined by ASTM C 1327-08 standard test method for Vickers indentation hardness of advanced ceramics were followed. Optical microscope measurements were performed promptly after indentations to reduce the possibility of crack growth. A series of N_i = 5 indentations were made for each applied load with an application time of 10 s. Samples were examined by SEM after measurement.

2.9 *RUS:* RUS measurements were collected on sintered rectangular parallelepipeds of $Yb_{14}MgSb_{11}$+ *x* volume % (*x* = 0, 8) composition using a commercial RUSpec system purchased from Quasar International.[37-38] A drive transducer sweeps across a frequency range of 100 - 400 kHz in 10 Hz steps, and two pick up transducers record peaks at the sample's resonant frequencies. Data were analyzed using commercial software (RPModel, Quasar International). The overall goodness-of-fit was calculated from the root-mean-square difference between the predicted and observed resonant frequencies and was less than 0.5% for both samples.

2.10 *Thermal conductivity:* Thermal diffusivity was measured on a Netzsch LFA 457 laser flash system from 298 K to 1273 K in 100 K increments. Sample disks were polished flat and coated with graphite for measurement. Thermal conductivity was calculated at the measured temperatures from $\kappa = D\ x\ C_P\ x\ \rho$ where D is measured diffusivity, C_p is heat capacity and ρ is density. Calculations were performed with the 'ATEC baseline' C_p of $Yb_{14}MnSb_{11}$ as reported previously with the following modifications:[15, 22, 39-40] C_p was adjusted for Fe content with the temperature dependent literature value of Fe's C_P[40] employing the rule of mixtures where the C_P of each component of the composite was multiplied by the mass % of that component to give the total C_P: C_p (total) = $(C_P\ Yb_{14}MnSb_{11} \times mass\ \%\ Yb_{14}MnSb_{11}) + (C_P\ Fe \times mass\ \%\ Fe)$. Temperature dependent density was calculated by using the coefficient of thermal expansion previously reported for $Yb_{14}MnSb_{11}$[41] and Fe[18] which was also scaled using the rule of mixtures. κ_l was calculated using the Wiedemann−Franz law for thermal conductivity ($\kappa_l = \kappa_{tot} -$

κ_e, $\kappa_e = \frac{1}{\rho} LT, L = 1.5 + e^{\left(\frac{|S|}{116}\right)} \times 10^{-8} \frac{W}{K^2\Omega}$).[5, 42] Raw diffusivity data are plotted in SI, Fig. S6. The resulting thermal conductivity data were fit with a sixth order polynomial for viewing ease and zT calculations.

2.11 *C_p and Thermogravimetry/differential scanning calorimetry (TG/DSC):* C_p adjustments via the rule of mixtures were confirmed by measuring the C_p of a sintered pellet of $Yb_{14}MgSb_{11}$ + 8 volume % Fe. The measurement was performed with a Netzsch STA 449 F3 equipped with a SiC furnace. After a blank and sapphire baseline were established, the flat pellet was placed into a graphite crucible and measured from 300 K to 1273 K under 50 mL/min of Ar at 20 K/min. TG/DSC was performed on a sintered pellet of $Yb_{14}MgSb_{11}$ + 8 volume % Fe employing a Netzsch Thermal Analysis STA 449 PC. After a blank baseline was established the flat pellet was placed into an alumina crucible and measured from 300 K to 1273 K under 50 mL/min of Ar at 20 K/min. The data were analyzed using the Netzsch Proteus analysis software.

2.12 *Hall effect and resistivity measurements:* Temperature-dependent resistivity and Hall coefficient were measured on flat disks a custom-built apparatus using the Van der Pauw method and a 0.8 T magnet with tungsten pressure contacts under high vacuum. Samples were heated at a rate of 180 K/h.[43] Data were fit with a sixth order polynomial for zT calculations and the fits are plotted in Results and Discussion. Experimental resistivity data are plotted in SI, Fig. S6.

2.13 *Seebeck measurements:* Seebeck measurements were performed on flat disks using a custom-built unit with tungsten-niobium thermocouples using the light-pipe method.[44] Data were fit with a sixth order polynomial for zT calculations and are plotted in Results and Discussion. Experimental Seebeck data are plotted in SI, Fig. S6.

3. Results and Discussion

3.1 *Synthesis, PXRD, and Rietveld Refinement:* Figure 2 shows a portion of the powder diffraction data for the $Yb_{14}MgSb_{11}$ composites prepared with *x* vol % Fe. The highlighted section of the graph shows the (110) peak of the body centered cubic (BCC) phase of Fe. This peak increases in intensity as the amount of Fe in the composite increases.

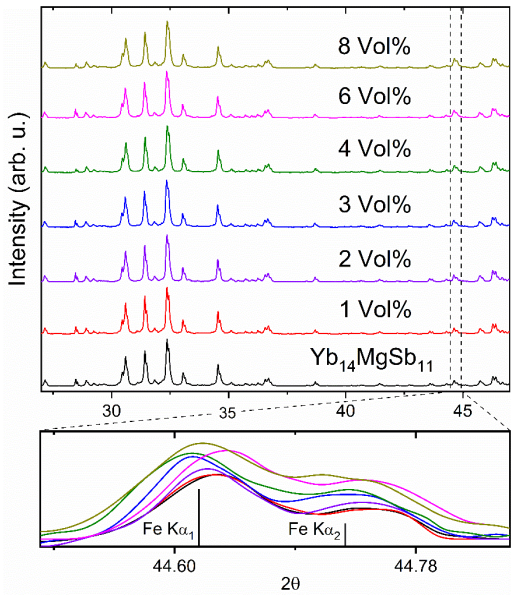

Figure 2. A portion of the PXRD pattern showing the observed pattern for composites prepared from micron-Fe with an expanded section from 44.5 - 44.8˚ showing the peaks assigned to Fe. The intensity is linear and normalized.

Table 1 summarizes lattice parameters and phase fractions from Rietveld refinement. The vol % Fe by Rietveld refinement shows that the vol % of Fe increases from 0, 1.71 (1), 1.61 (2), 2.77 (3), 3.81 (4), 4.44 (6), 7.74 (8) (refined fraction, (loaded fraction)) consistent with the nominally loaded volume % of Fe. Small amounts of both $Yb_{11}Sb_{10}$ and Yb_2O_3 are identified as minor impurity phases in the samples. $Yb_{11}Sb_{10}$ is a metallic phase with a small Seebeck coefficient, low electrical resistivity, and increased thermal conductivity compared with $Yb_{14}MgSb_{11}$.[45] $A_{11}Pn_{10}$ is a common impurity in $A_{14}MSb_{11}$ samples when prepared from the elements and its influence has been reported to be minimal for amounts less than 10%.[15, 20, 22, 46] The mass % of $Yb_{11}Sb_{10}$ in the sample without Fe is 5.29 %, however, samples with Fe inclusions do not exceed ~3 mass %. As the amount of Fe in the samples increases, the amount of $Yb_{11}Sb_{10}$ decreases until the 3 volume % composite where 2.04 mass % $Yb_{11}Sb_{10}$ is present.[45] These composite samples are prepared from the same starting batch of $Yb_{14}MgSb_{11}$ and are processed the same way, so it appears that Fe acts as a grinding aid which enables Mg to be more evenly distributed in the pre-reacted powder leading to less $Yb_{11}Sb_{10}$ after reaction and densification. The $Yb_{11}Sb_{10}$ concentration in the samples is around that reported for furnace annealed powders after SPS (1.47 mass % $Yb_{11}Sb_{10}$) in $Yb_{14}MnSb_{11}$ and less than what has been reported after SPS in $Yb_{14}MgSb_{11}$ (unquantified, less than 5 mass %).[15, 22-23]

The volumes of the unit cells vary by less than 2 $Å^3$ and the patterns calculated from

$Yb_{14}MgSb_{11}$ fit the data well.[22] The lattice parameters and volume of the unit cell are slightly larger than that previously reported by Hu, et al. and closely follow that of Justl, et al. where MgH_2 is used as the Mg source.[15, 23]

Table 1. Reported Lattice Parameters for $Yb_{14}MgSb_{11}$ and Rietveld Refinement Results of $Yb_{14}MgSb_{11}$ Composites.

Sample	***a* (Å)**	***c* (Å)**	**V (Å^3)**	**Temp. (K)**	**λ (Å)**	**Space group**
$Yb_{14}MgSb_{11}$[15]	16.602(1)	22.233(1)	6128.0(6)	293	1.5406	*I*4$_1$/*acd*
$Yb_{14}MgSb_{11}$ (MgH_2 source)[23]	16.6081(1)	22.2436(1)	6315.5(1)	293	1.5406	*I*4$_1$/*acd*
		Fe source: Micron-Fe				
$Yb_{14}MgSb_{11}$	16.6075(5)	22.2486(12)	6136.3(4)			
+1 vol. %Fe	16.6099(4)	22.2493(9)	6138.3(3)			
+2 vol. %Fe	16.6092(4)	22.2467(8)	6137.0(3)			
+3 vol. %Fe	16.6109(4)	22.2480(9)	6138.7(4)			
+4 vol. %Fe	16.6117(4)	22.2496(9)	6139.7(3)			
+6 vol. %Fe	16.6106(5)	22.2479(10)	6138.4(4)	293	1.5406	*I*4$_1$/*acd*
+8 vol. %Fe	16.6115(5)	22.2483(11)	6139.2(4)			

Sample	**$Yb_{14}MgSb_{11}$ (Wt. %)**	**$Yb_{11}Sb_{10}$ (Wt. %)**	**Yb_2O_3 (Wt. %)**	**Fe (Wt.%)**	**Fe (Vol. %)**	**wRp (%)**	**GOF**
$Yb_{14}MgSb_{11}$	93.7(5)	5.29(13)	1.03(4)	N/A	N/A	8.28	1.89
+1 vol. %Fe	96.9(4)	0.70(8)	0.59(4)	1.77(1)	1.71(1)	7.82	1.85
+2 vol. %Fe	96.9(4)	0.70(1)	0.59(4)	1.7(1)	1.6(1)	7.93	1.56
+3 vol. %Fe	94.6(4)	2.04(8)	0.48(2)	2.87(1)	2.77(1)	7.56	1.71
+4 vol. %Fe	94.6(4)	1.051(9)	0.33(3)	3.94(1)	3.81(1)	8.06	1.80
+6 vol. %Fe	92.9(3)	2.00(9)	0.48(3)	4.6(1)	4.4(1)	7.50	1.68
+8 vol. %Fe	88.6(4)	2.8(1)	0.5(1)	8.02(2)	7.74(2)	8.75	2.07

The refinement of the X-ray powder diffraction data does not allow for refinement of small amounts of Fe substituted on atomic positions. Following similar mechanical milling and SPS densification as described for $Yb_{14}MgSb_{11}$ except employing Fe to replace Mg, the synthesis of $Yb_{14}FeSb_{11}$ was attempted (SI, Fig. S7). The phase did not form indicating Fe does not dope into $Yb_{14}MgSb_{11}$.

3.2 *SEM and EMPA*: The $Yb_{14}MgSb_{11}$ composites were imaged in backscatter electron (BSE) (Z-contrast) mode before and after thermoelectric property measurement. Figure 3 shows BSE images for the x = 0, 4, 8 volume % Fe composites with the remainder in the SI, Figure S8.

The pristine $Yb_{14}MgSb_{11}$ sample shows some pullout marks from polishing, but the uniform matrix is consistent with phase pure sample. The 4 volume % composite shows elongated dark marks corresponding to Fe; the same features are more pronounced in the 8 volume % sample. The $Yb_{14}MgSb_{11}$ matrix and the Fe are well segregated suggesting no reaction at the grain boundaries. Also, the images before and after cycling are very similar indicating the Fe is not diffusing or reacting with the $Yb_{14}MgSb_{11}$ matrix upon heating, similar to what was seen by Cerretti, et al. [47] when compositing W with $Yb_{14}MnSb_{11}$. ImageJ analysis using default threshold values calculate the average size of the black spots in all of the composite samples to be 1 μm. [2,28]

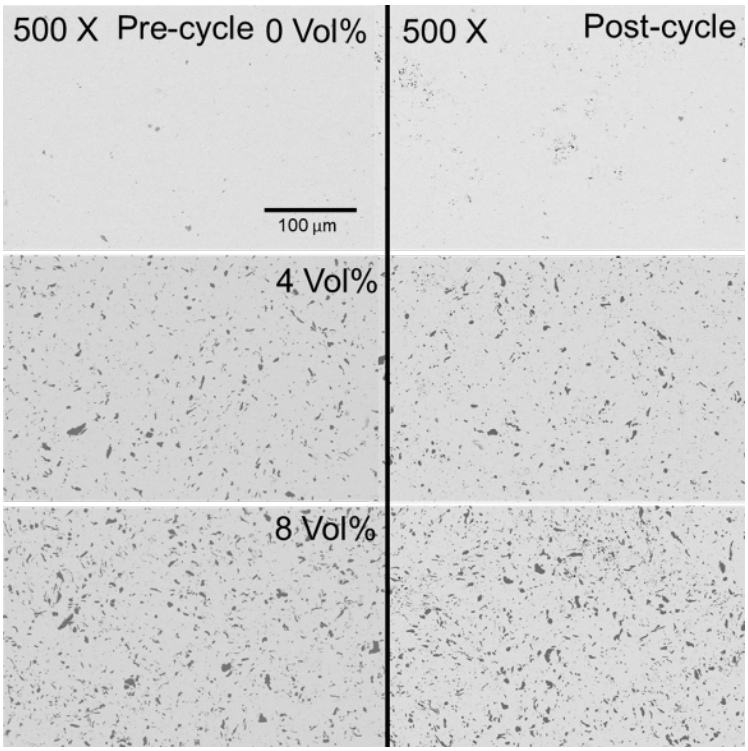

Figure 3. Backscattered electron images (Z contrast) at 500x of $Yb_{14}MgSb_{11}$ + 0, 4, 8 volume % Fe composites before and after cycling to 1273 K three times.

The composition calculated from EMPA analysis for $Yb_{14}MgSb_{11}$ is basically unchanged before and after thermal cycling with $Yb_{13.93(6)}Mg_{1.10(4)}Sb_{10.97(7)}$ before and $Yb_{13.95(10)}Mg_{1.04(4)}Sb_{10.99\,(10)}$ after. Figure 4 shows the X-ray mapping for $Yb_{14}MgSb_{11}$ + 1, 4 volume % Fe from micron-Fe samples before and after thermal cycling. There are areas of zero

Fe concentration and scattered areas of medium and high Fe concentration indicating that Fe is well isolated. Similar to the BSE images, there is no evidence for Fe diffusion after cycling.

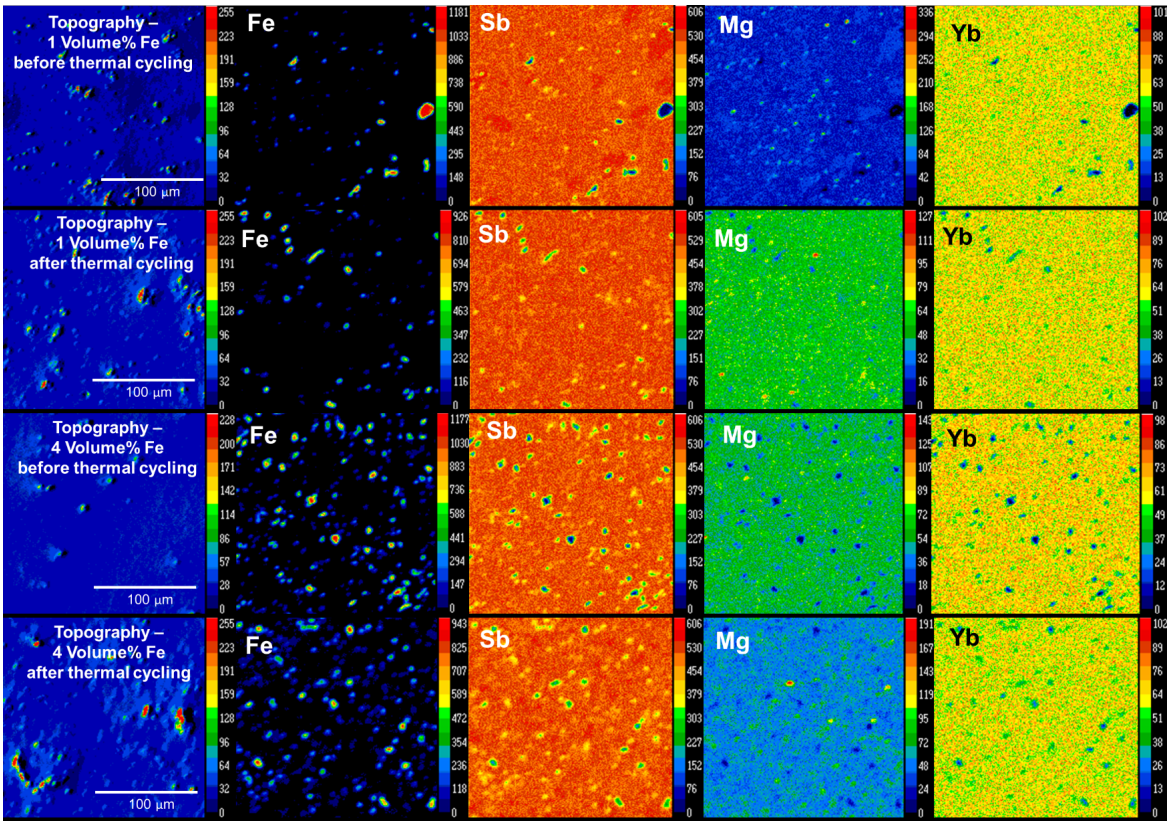

Figure 4. EMPA topological images and X-ray elemental maps for $Yb_{14}MgSb_{11}$ + 1 and 4 volume % Fe composites before and after thermal cycling.

3.3 *FORC:* To study the interactions between the Fe clusters inside the samples, we have analyzed the FORC distributions in the (H_C, H_B) space. Figure 5(A) shows the FORC distributions for $Yb_{14}MgSb_{11}$ composites with varying Fe content. There are two primary features in the FORC distributions. The first is a vertical ridge along the bias field H_B axis, with a large spread of up to $\pm$ 6kOe, and mostly confined to H_C < 1 kOe. This type of vertical ridge in H_B is characteristic of particle systems with strong demagnetizing dipolar interactions.[32, 48] The second feature in the FORC diagrams is a horizontal tail near $H_B = 0$ that extends up to $H_C \sim 4$ kOe, indicating that a fraction of the particles exhibit much larger coercivities. The narrow distribution of this tail along $H_B = 0$ suggests that these high coercivity particles are essentially non-interacting and switching independently. Furthermore, we have evaluated the FORC distribution onto the H_B axis, by integrating along the H_C axis, to obtain the bias field

distribution, and determined their full-width-at-half-maximum (FWHM), as shown in Figure 5(B) and 5(C), respectively. The bias field distribution measures the strength of the magnetic interaction between the Fe particles. For non-interacting particles, a narrow peak centered at H_B= 0 is expected.[34] As the interaction increases, the peak will become broader, manifested in its FWHM. Even though all samples exhibit a strong dipolar interaction between the particles, with increasing Fe content, the FORC projection becomes more spread out along the H_B axis and the FWHM increases. This suggests that adjacent Fe particles are becoming larger and /or closer together, leading to increased dipolar interactions. This interpretation is consistent with the SEM images (Fig. 3), showing the average spacing between adjacent Fe particles getting smaller with increasing Fe concentration, hence stronger dipolar interactions. Additionally, had Fe been incorporated into the $Yb_{14}MgSb_{11}$ structure, we would expect to observe a qualitative deviation from this FORC distribution, due to the presence of additional magnetic phase and potentially long-range magnetic interactions. This would have been manifested as additional features in the FORC diagram or an asymmetric FORC distribution along the H_B axis, respectively.[49] The absence of such deviation suggests that the Fe is not incorporated into the structure.

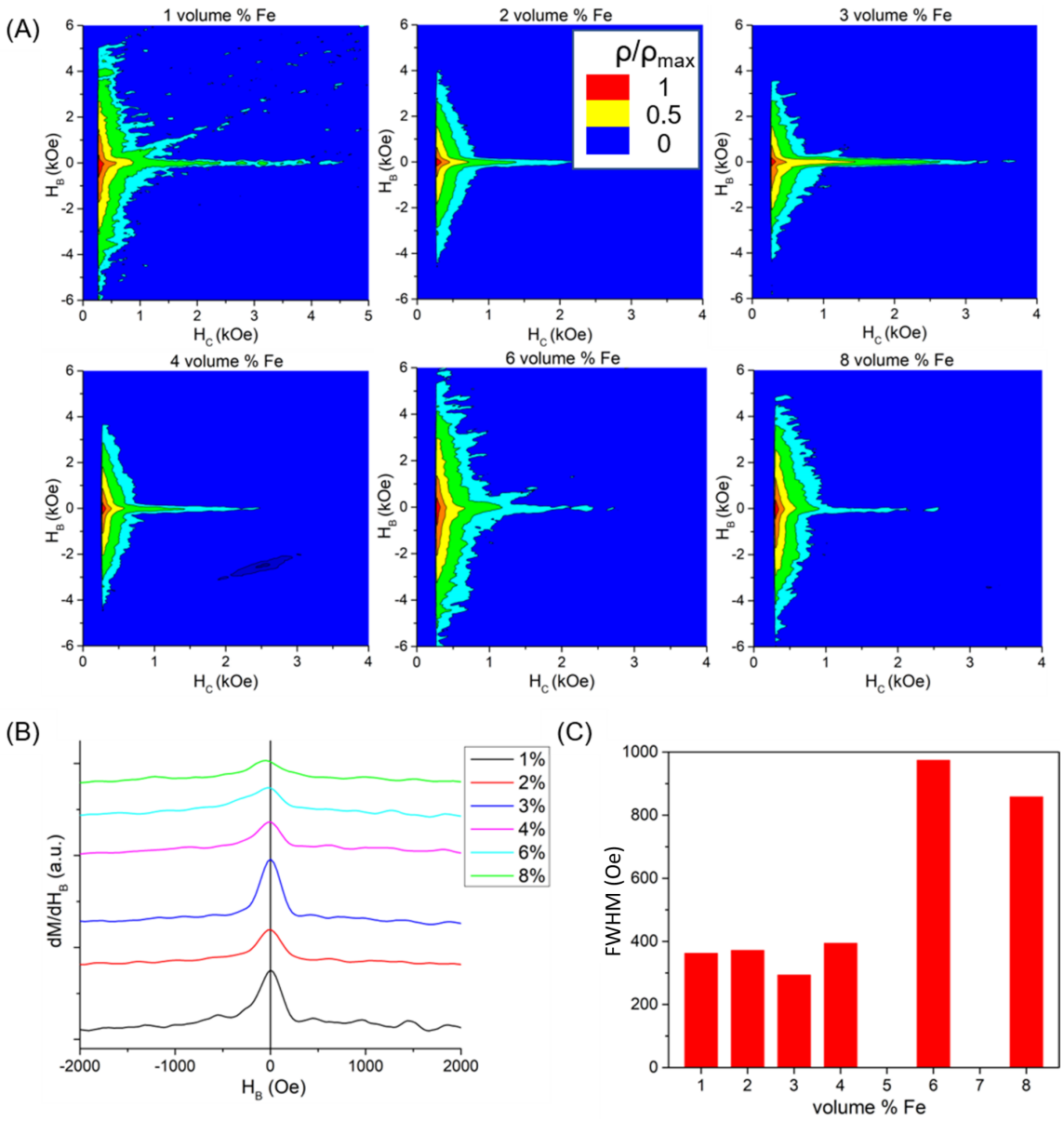

Figure 5. (A) FORC distribution for $Yb_{14}MgSb_{11}$ composites with varying Fe volume concentration. (B) Bias field distribution of the samples extracted by the projection of the FORC distributions in (A) onto the H_B axis. (C) FWHM of the bias field distributions shown in (B).

3.4 *TEM:* In order to further investigate the nature of Fe in the composite a TEM sample was prepared from a 1 volume % Fe (micron-Fe) composite. From the HAADF-STEM image and corresponding EDS mapping shown in Figure 6, several Fe-rich sites in the $Yb_{14}MgSb_{11}$ structure are located, shown in red in the EDS map. The size of such segregated Fe phase is about 200 nm in diameter. It also shows that the Yb, Mg, and Sb are homogeneously distributed over the whole region. In order to compare the compositional information at different locations

on the specimen, 3 different regions (Area #1, #2 and #3) were selected in the HAADF-STEM image and the elemental spectral information extracted. Specifically, Area #1 is the Fe-rich site, and Area #2 and Area #3 are chosen from the Fe-deficient sites. From the corresponding elemental mapping and the spectral data, it's clear that Fe can be only identified at area #1, while areas #2 and #3 only show Yb, Mg, O, and Sb. The oxygen peak was present in area #2 but not in area #3, indicating that the oxygen is at the surface of the specimen and is not a constituent in the original sample. The oxygen peak is attributed to surface oxidation that occurred during the sample preparation process.

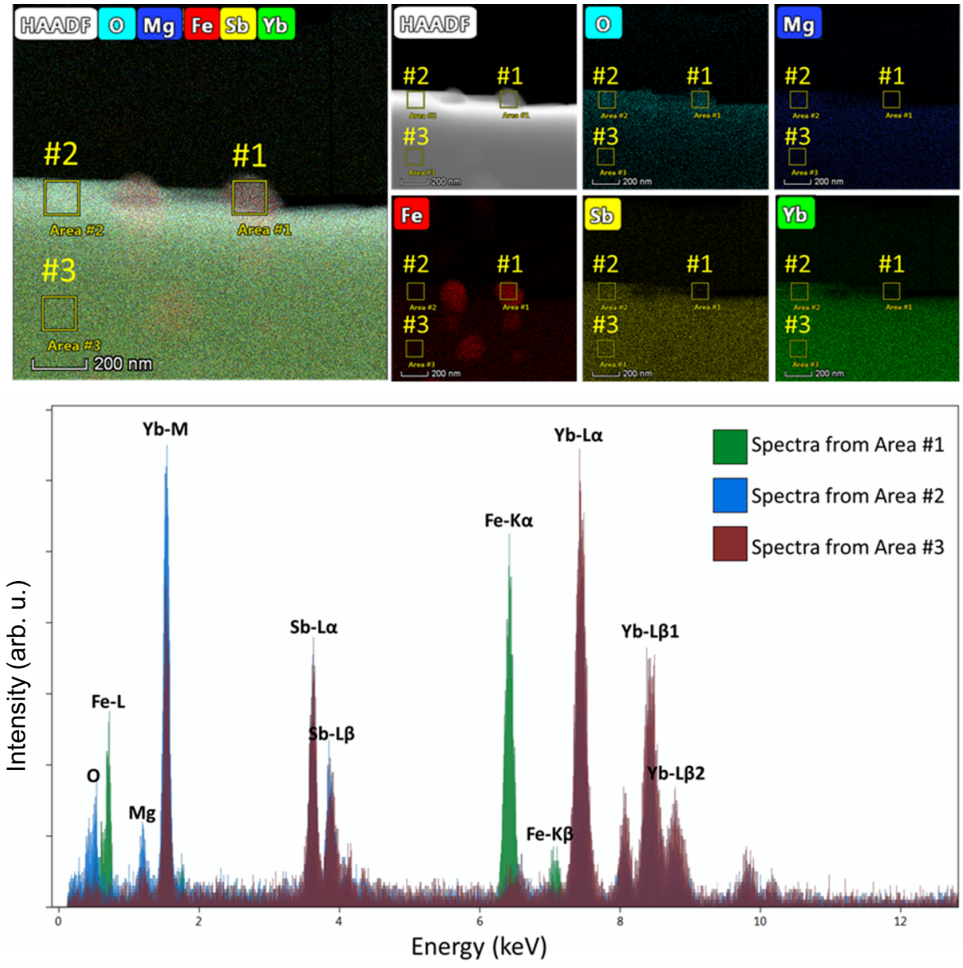

Figure 6. STEM-EDS elemental mapping and corresponding spectrum from selected area in the HAADF STEM image.

3.5 *Mechanical Properties*: Composite samples are qualitatively robust when handling, cutting and polishing. To probe the mechanical properties $Yb_{14}MgSb_{11}$ and $Yb_{14}MgSb_{11}$ + 8 volume % Fe composite were probed with a Vickers hardness test microindenter. The

composited samples did not show significant increase in hardness (SI, Fig. S4) but when samples without Fe are indented (Fig. 7 (A)) long non-deflected cracks are seen. When Fe containing samples are indented crack arresting is observed at Fe inclusions (Fig. 7 (B)) indicating that the composited samples are tougher than non-composited samples. The same behavior is seen in 4 volume % Fe samples (SI, Fig. S5) potentially indicating that the toughening mechanism may be at play for all compositions in the series.

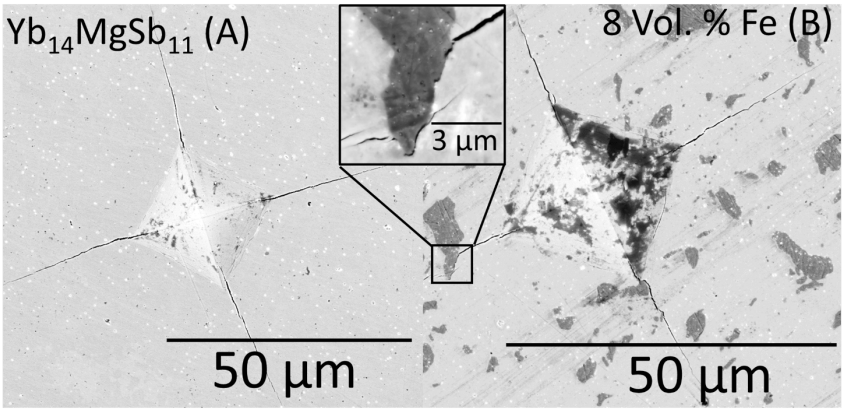

Figure 7. Long cracks can be seen in the sample with no Fe (A). In the sample with 8 volume % Fe (B) the crack is arrested by an Fe inclusion (enlarged region).

RUS: RUS results are summarized in Table 2 along with literature values for longitudinal and shear constants measured on roughly rectangular single crystals of $Yb_{14}MnSb_{11}$.[50] RUS results show $Yb_{14}MgSb_{11}$ has roughly the same longitudinal and shear constants as $Yb_{14}MnSb_{11}$ and the 8 volume % composite is stiffer than either $Yb_{14}MnSb_{11}$ and $Yb_{14}MgSb_{11}$. The 8 volume % composite has increased Bulk, Shear, and Young's modulus along with an increase in longitudinal and shear speeds of sound. This suggests that Fe compositing gives $Yb_{14}MgSb_{11}$ a mechanical advantage when it comes to withstanding the large axial compression the thermoelectric material will experience in a device. The increased moduli are expected to be a function of Fe loading, and we expect that the larger Fe concentration should have the largest effect from inclusions.

Table 2. Results of RUS Measurements on $Yb_{14}MgSb_{11}$ and $Yb_{14}MgSb_{11}$ + 8 volume % Fe composite and elastic constants reported for $Yb_{14}MnSb_{11}$[50] and measured on $Yb_{14}MgSb_{11}$ and the 8 volume % composite.

Sample	$v_{longitudinal}$	v_{shear}	Bulk Modulus	Shear Modulus	Young's Modulus	Poisson's ratio
$Yb_{14}MgSb_{11}$	3076 m/s	1796 m/s	41.53 GPa	25.96 GPa	64.45 GPa	0.241
$Yb_{14}MgSb_{11}$ + 8 Vol. % Fe	3262 m/s	1879 m/s	47.83 GPa	28.44 GPa	71.21 GPa	0.252
	Reported for $Yb_{14}MnSb_{11}$[50]	$Yb_{14}MgSb_{11}$	$Yb_{14}MgSb_{11}$ + 8 Vol. % Fe			
C_{11} (GPa)	72.5	76.14	85.75			
C_{44} (GPa)	25.1	25.95	28.44			

3.6 *Heat Capacity and Thermal Stability*: The efficacy of C_P calculations from literature values by the rule of mixtures ($(C_P\ Yb_{14}MnSb_{11} \times mass\ \%\ Yb_{14}MnSb_{11}) + (C_P\ Fe \times mass\ \%\ Fe)$[39-40]) was ensured by measuring the C_P of the 8 Volume % composite. Figure 8 shows that the measured C_p and the calculated C_p are in good agreement. It is assumed the C_P of the other composites would also follow from the rule of mixtures. Thermal stability of the 8 volume % Fe composite was investigated by TG/DSC. The TG curve (Fig. 8) shows negligible mass gain/loss. The phase stability is in agreement with the reported TG/DSC data for $Yb_{14}MgSb_{11}$.[15] There is a slight downturn in DSC signal (SI, Fig. S9) at 1043 K which is attributed to the Curie point of Fe.[18]

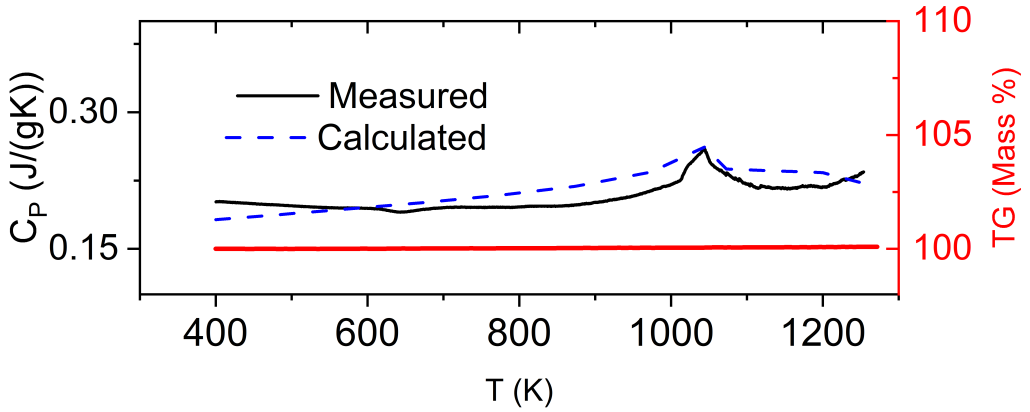

Figure 8. Measured (black line) and calculated C_p (blue dashed line) of $Yb_{14}MgSb_{11}$ + 8 volume % Fe composite collected at 20 K/min and TG of $Yb_{14}MgSb_{11}$ + 8 volume % Fe. The measured C_p data shows good agreement with C_p calculated from rule of mixtures. The composite shows no mass loss upon heating to 1273 K.

3.7 *Thermal Conductivity:* Figure 9 shows κ_{tot} and κ_l vs temperature for the composite samples. The thermal conductivity for $Yb_{14}MgSb_{11}$ at 1073 K is 7.05 mW/cm-K which is consistent with that reported in the literature (7.1, 7.2 mW/cm-K).[15, 23] All samples show κ_l and κ_{tot} increasing as volume % Fe increases. Effective Medium Theory (EMT) was used to model the thermal conductivity of $Yb_{14}MgSb_{11}$ composited with Fe using the Maxwell-Euken (ME3) equation.[51] At low Fe concentrations the thermal conductivity closely follows the EMT model, but as Fe increases the thermal conductivity deviates. EMT scales κ_{tot} as a function of volume % Fe, but SEM and FORC show the particles are larger, more interacting, and closer together as Fe content increases thereby increasing κ_{tot} more than expected, therefore EMT may be too simplistic to model the higher volume % composites. This deviation of the EMT model has also been reported by Cerretti, et al. [47] when compositing W with $Yb_{14}MnSb_{11}$ and is explained as a deviation from Boltzmann transport theory. SEM (Fig. 3) shows that the Fe particles are over 1 μm on average, therefore the Fe inclusions likely do not provide enough phonon scattering to reduce thermal conductivity as is evident from the κ_l instead they act like thermal shunts that increase both κ_l and κ_{tot}. This increase in κ_l is consistent with the speed of sound measurements, which increase as a function of the volume fraction of Fe. This further suggests that the size of the particles is much greater than the average phonon mean free path and thus do not significantly scatter phonons.

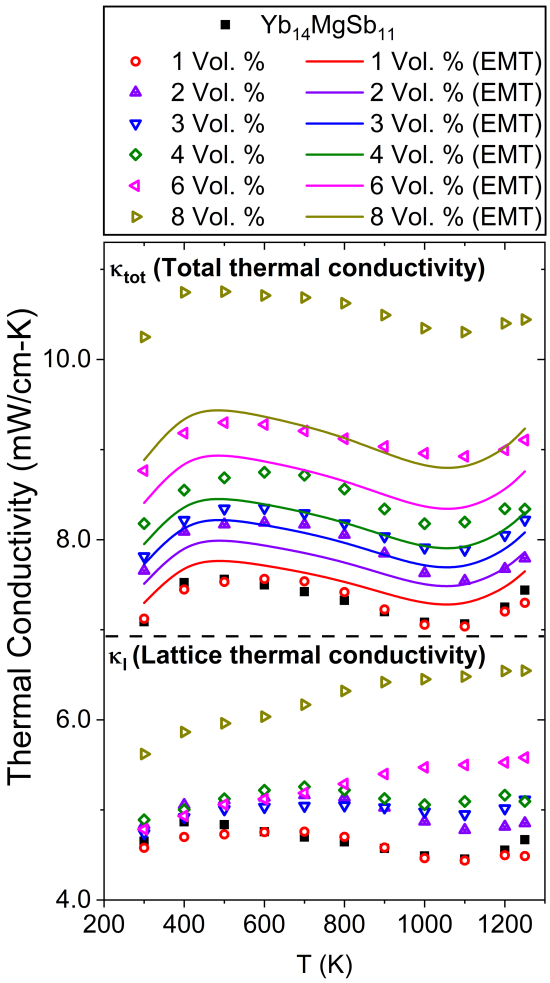

Figure 9. κ_{tot} and κ_l conductivity vs temperature for $Yb_{14}MgSb_{11}$ composites. The solid lines represent the thermal conductivity predicted by EMT. The dashed line marks the change from κ_{tot} to κ_l.

3.8 *Resistivity:* Figure 10 shows resistivity vs temperature for the composite samples. $Yb_{14}MgSb_{11}$ has a resistivity of 7.05 mΩ-cm which is comparable to literature values at 1073 K (8.2, 6.75 mΩ-cm).[15, 23] All composites show similar temperature dependent behavior and as the Fe volume % increases the resistivity decreases. EMT calculations predict that the resistivity will be higher than the measured values which is opposite of the trend in thermal conductivity which may also be attributed to the changing size and shape of the Fe particles. The gradual reduction in electrical resistivity as a function of the low volume % Fe is a deviation from percolation theory which predicts a constant resistivity until ~18 volume % inclusion at which point a large reduction in resistivity will take place.[52] Cheikh, et al.[9] observe a similar reduction in resistivity in $LaTe_{1.46}$ composited with Ni.[9] Using Monte Carlo simulations, they theorize that Ni is creating conductive pathways through the material, reducing resistivity at volume

percentages that are lower than expected by percolation theory, and coined the term "composite assisted funneling of electrons" (CAFE) to describe the effect.[9] We hypothesize that CAFE is also taking place in $Yb_{14}MgSb_{11}$ + x volume % Fe.

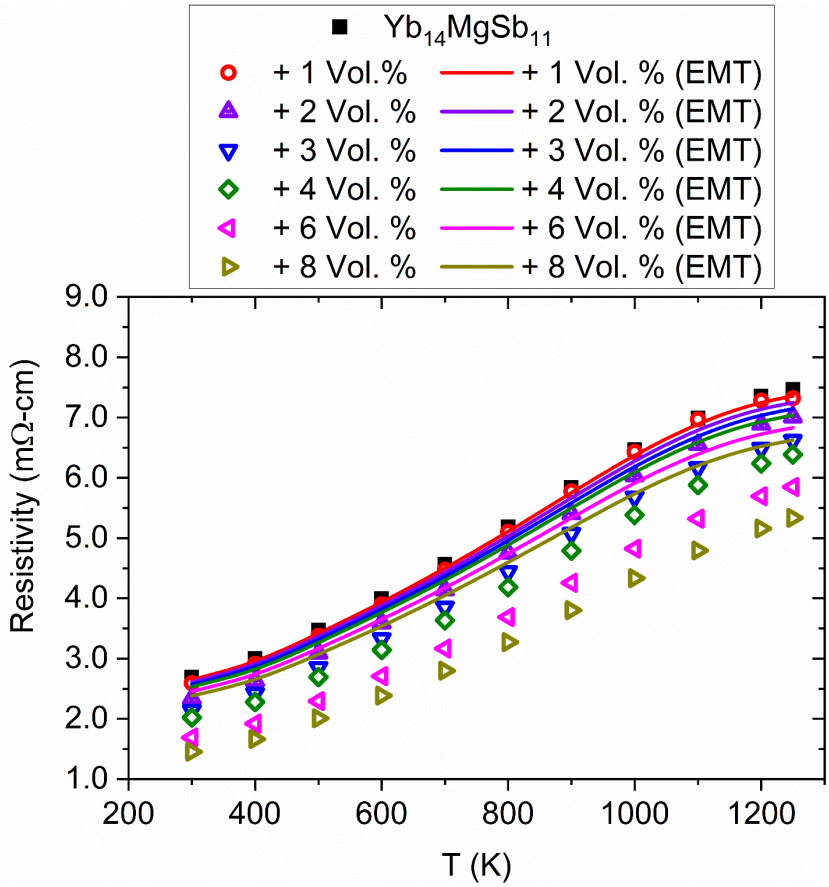

Figure 10. Resistivity and vs temperature for $Yb_{14}MgSb_{11}$ composites. The solid lines represent the resistivity predicted by EMT.

3.9 *Seebeck:* The Seebeck coefficient vs temperature for composites samples are provided in Figure 11. The inlay shows the values at peak zT (1200 K). $Yb_{14}MgSb_{11}$ has a Seebeck coefficient of 210 μV/K at 1073 K which is lower than the reported values of 236, 220 μV/K.[15, 23] The 3 volume % composite has the peak Seebeck of 230 μV/K at 1200 K and all samples are within 7% of this value. The value of the Seebeck coefficients for all samples are well within error of the measurement (~7%) indicating that the carrier concentration of the samples is not significantly affected by the presence of Fe.[53] This is useful because as confirmed by FORC, magnetically active Fe particles are in the samples and carrier concentration data from Hall measurements below the Curie temperature of Fe (1043 K) (SI, Fig. S10, S11) are known to be anomalous.[18, 54] Above the Curie temperature the value of the Hall mobility is below 1 cm^2/Vs

which leads to noisy carrier concentration characteristic of low mobility systems.[43] The large reduction in resistivity without a significant change in Seebeck coefficient was also seen by Cheikh, et al.[9] in $LaTe_{1.46}$. The large difference in thermal conductivity of Fe compared to $Yb_{14}MgSb_{11}$ causes Fe inclusions to act like thermal shunts with small thermal gradients in them, so from an electronic point of view Fe inclusions act like voids, which are known to have virtually no effect on bulk Seebeck coefficient of a material.[55]

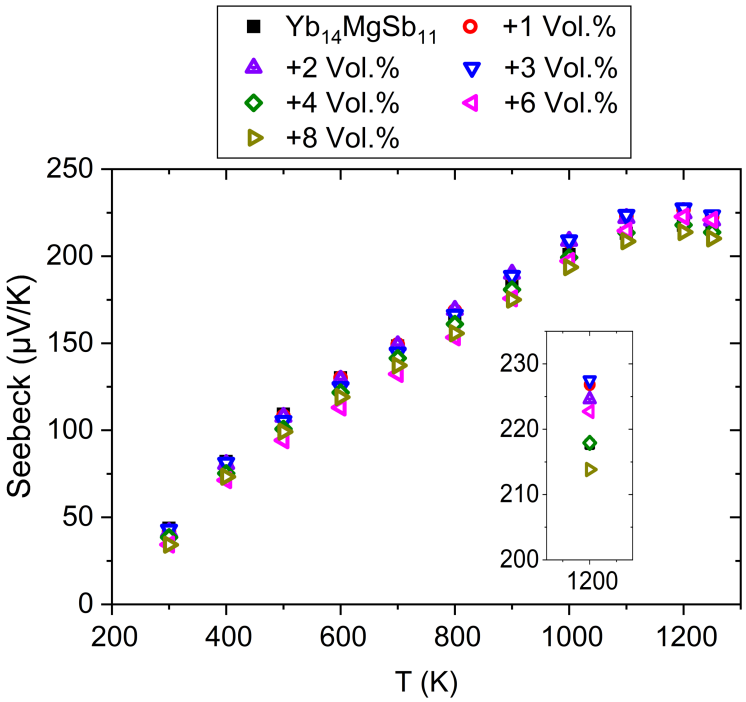

Figure 11. Seebeck vs temperature for $Yb_{14}MgSb_{11}$. The inlay shows the Seebeck coefficient at 1200 K.

3.10 *Power Factor (PF) and Property Analysis:* The PF (Fig. 12) of the composites, with the exception of the 3 volume % Fe sample, increases with increasing Fe. The best composite with respect to PF is the 8 volume % Fe composite which has a 40% increase in PF at 1100 K compared to the $Yb_{14}MgSb_{11}$ phase.

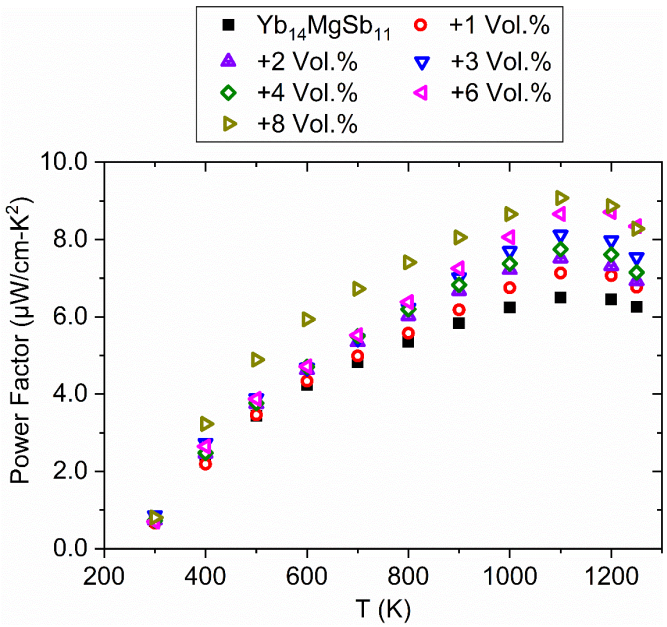

Figure 12. Power Factor vs temperature for $Yb_{14}MgSb_{11}$ composites.

Figure 13 shows the percent change in stated property as a function of volume % Fe for thermoelectric properties at 1200 K. When the percent change of resistivity and thermal conductivity of the composites are added the value never goes above 2% until the 8 volume % Fe sample. The Seebeck coefficient is maintained for all of the composites except the 8 volume % indicating that zT at 1200 K is improved in all composites except the 8 volume %. The large reduction in resistivity for that composition explains the increase in PF.

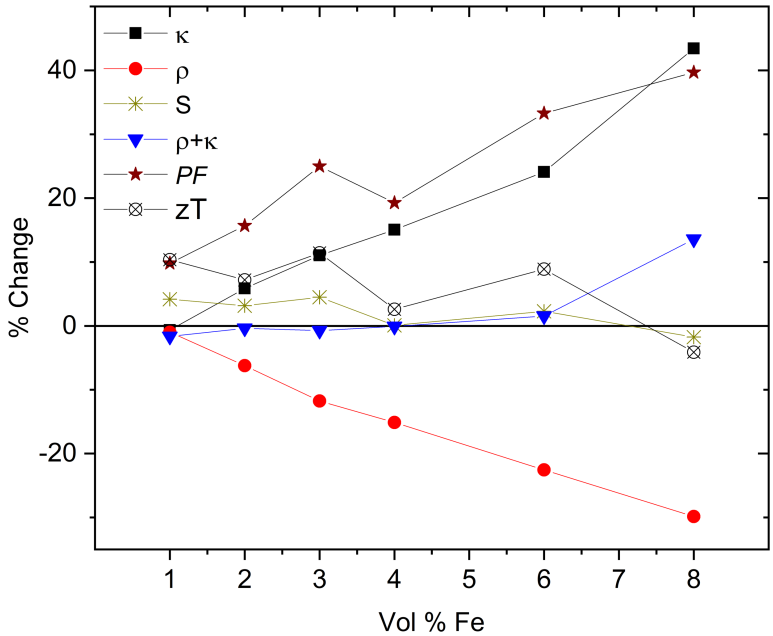

Figure 13. Percent change of κ, ρ, and PF compared to $Yb_{14}MgSb_{11}$ as a function of Fe volume % at 1200 K and the sum of ρ and κ (PF is at 1100 K).

3.11 *zT:* Figure 14 shows the zT vs temperature for the composites and $Yb_{14}MgSb_{11}$. $Yb_{14}MgSb_{11}$ has a zT of 0.98 at 1073 K which is close to the value reported by Hu, et al.[15] of 1.02 and smaller than the value reported by Justl, et al.[23] *of* 1.15. The best composite is the 3 volume % Fe sample with a peak zT of 1.18 at 1200 K and a zT of 1.10 at 1073 K due to increased PF.

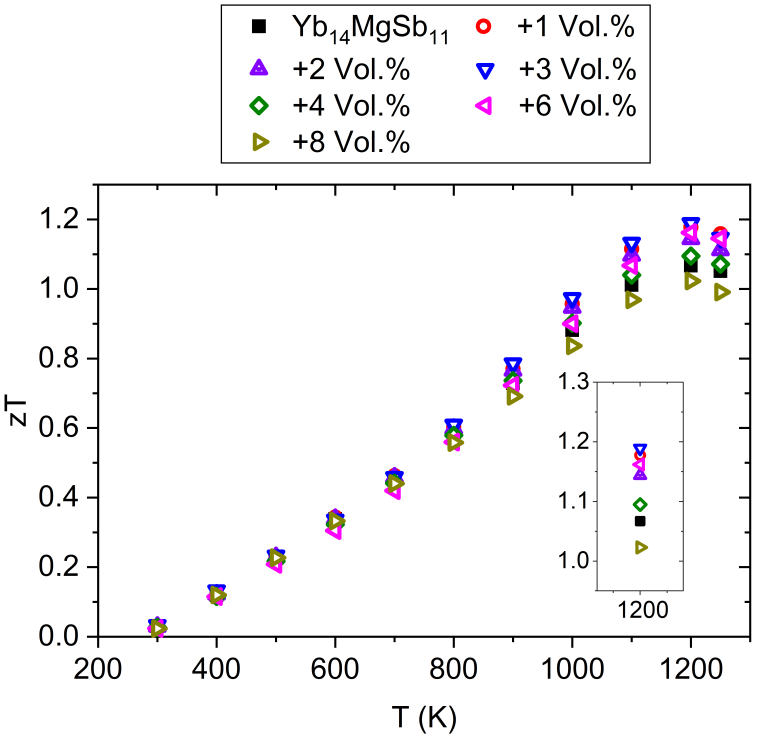

Figure 14. zT vs temperature for $Yb_{14}MgSb_{11}$ composites. The inlay shows the zT at peak performance (1200 K).

3.12 *Compatibility factor:* In order to keep a high zT across a wide temperature range and maximize the Carnot efficiency of a thermoelectric generator, materials with high zTs at given temperatures are coupled together. Coupling $Ce_{0.9}Fe_{3.5}Co_{0.5}Sb_{12}$ (peak zT at 850 K) and $Yb_{14}MnSb_{11}$ (peak zT at 1273 K) by the ATEC project has shown to increase the efficiency of a thermoelectric generator.[1, 56] Figure 15 shows the compatibility factor for $Yb_{14}MgSb_{11}$ composites and $Ce_{0.9}Fe_{3.5}Co_{0.5}Sb_{12}$.[56] All of the samples are within 2 V^{-1} of $Ce_{0.9}Fe_{3.5}Co_{0.5}Sb_{12}$ indicating all of the composites can be segmented with $Ce_{0.9}Fe_{3.5}Co_{0.5}Sb_{12}$.

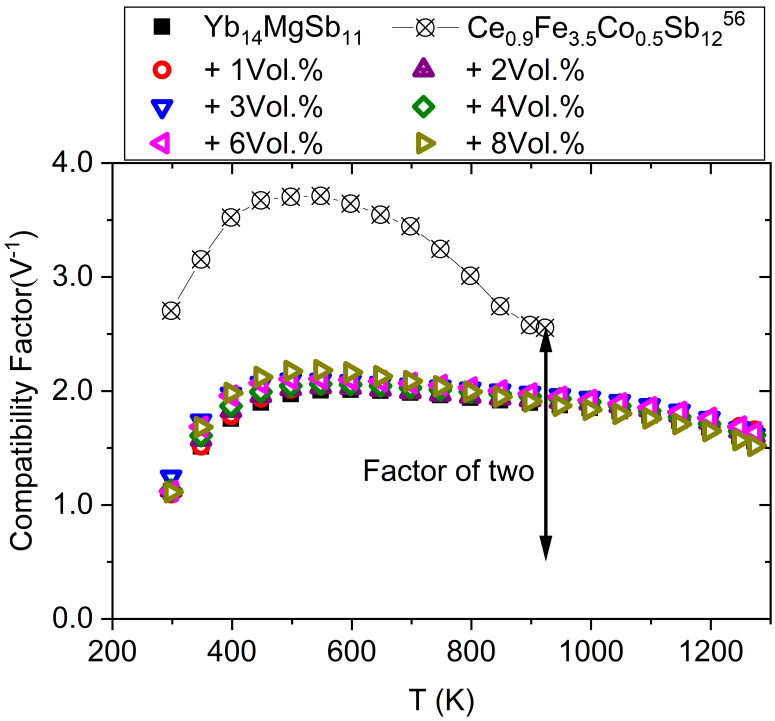

Figure 15. Compatibility Factor calculated from literature values of $Ce_{0.9}Fe_{3.5}Co_{0.5}Sb_{12}$[56] and from thermoelectric data of $Yb_{14}MgSb_{11}$.

4.1 *Conclusions:* $Yb_{14}MgSb_{11}$+ *x* volume % Fe composites have been synthesized via a fast, scalable, mechanical milling and SPS process with (6-10 μm) micron-Fe. A collective array of microscopies and diffraction show that Fe inclusions are pure Fe and there is no evidence for diffusion or chemical reactions at the grain boundaries of $Yb_{14}MgSb_{11}$. FORC diagrams show strong dipolar interaction between particles. The composites are stable up to 1273 K and the morphology of the Fe does not change upon thermal cycling. The samples are qualitatively more robust than pristine $Yb_{14}MgSb_{11}$ and crack arresting caused by Fe inclusions is observed. RUS measurements showed the all of the elastic moduli of the 8 volume % Fe composite increase over $Yb_{14}MgSb_{11}$ providing some stiffening suggesting that Fe compositing gives $Yb_{14}MgSb_{11}$ the ability to withstand the large axial compression the thermoelectric material will experiences in a device. The inclusions of Fe in $Yb_{14}MgSb_{11}$ reduce resistivity slightly more than the simultaneous increase in thermal conductivity up to 4 volume % Fe leading to a peak zT of 1.18 in the 3 volume % Fe composite at 1200 K, an improvement of 11% over $Yb_{14}MgSb_{11}$ prepared in the same manner (1.06 at 1200 K). The 8 volume % Fe composite shows a large decrease in resistivity compared to pristine $Yb_{14}MgSb_{11}$ leading to a 40% improvement in PF. The

compatibility factor of the full range of $Yb_{14}MgSb_{11}$ + 1, 2, 3, 4, 6, 8 volume % Fe are within a factor of 2 V^{-1} of $Ce_{0.9}Fe_{3.5}Co_{0.5}Sb_{12}$ indicating all of the composites can be segmented with the lower temperature thermoelectric $Ce_{0.9}Fe_{3.5}Co_{0.5}Sb_{12}$ phase for optimal device efficiency.[56] Overall, $Yb_{14}MgSb_{11}$ + 3 volume % Fe provides the best material for compositing because of its presumed superior mechanical properties, superior zT, and higher PF compared to pristine $Yb_{14}MgSb_{11}$.[14]

5.1 *Acknowledgements:* This work was supported by NEUP and the NASA Science Missions Directorate's Radioisotope Power Systems Program. This work was performed in part at the Jet Propulsion Laboratory, California Institute of Technology under contract with the National Aeronautics and Space Administration. Z.J.C. and K.L. acknowledge support from the NSF (ECCS-1611424 and ECCS-1933527). Work at the Molecular Foundry was supported by the Office of Science, Office of Basic Energy Sciences, of the U.S. Department of Energy under Contract No. DE-AC02-05CH11231. This work was inspired by the findings of Samad Fridosy under the Advanced Thermoelectric Converter (ATEC) Project a division of the Thermal Energy Conversation Technologies group. The acquisition of a Magnetic Property Measurements System (MPMS3) at GU which was used in this investigation was supported by NSF Grant No. DMR-1828420. We would like to thank George Nakatsukasa, Gregory Gerig, and Dr. Dean Cheikh for their work measuring thermal conductivity, Seebeck coefficients, and heat capacity; Dr. Kathleen Lee for providing Mg_3Sb_2 precursor and helpful discussion on synthetic techniques; Dr. Fivos Drymiotis and Obed Villalpando for assistance with RUS and Vickers hardness measurements; and Dr. Julius De Rojas and Dr. Peyton Murray for assistance and helpful discussions on the FORC studies.

6. *Supporting information:* The Supporting Information is free of charge on the ACS publication website at DOI: XX.XXXX/acs.XXXXXX

PXRD of Mg_3Sb_2; A picture of the tungsten carbide endcap with Yb adhered to it; Rietveld refinement of $Yb_{14}MgSb_{11}$ + 0, 1, 2, 3, 4, 6, 8 volume % Fe; Results of Vickers hardness; SEM image of the 4 volume % Fe composite after indenting with 1000 gf; raw diffusivity, Seebeck and resistivity data; PXRD of an attempt to make $Yb_{14}FeSb_{11}$; SEM of $Yb_{14}MgSb_{11}$ + 0, 1, 2, 3, 4, 6, 8 volume % Fe before and after thermal cycling; DSC of the 8 volume % composite; Fit and raw carrier concentration and Hall mobility data. (PDF-13 pages)

References:

1. Fleurial, J.-P.; Bux, S.; Caillat, T., Engineering of Novel Thermoelectric Materials and Devices for Next Generation, Long Life, 20% Efficient Space Power Systems. In *11th International Energy Conversion Engineering Conference*, Thermoelectric Devices and Systems: Thermoelectric Devices and Systems, 2013.
2. Snyder, G. J.; Toberer, E. S., Complex thermoelectric materials. *Nat Mater* **2008,** *7* (2), 105-114.
3. Zeier, W. G.; Zevalkink, A.; Gibbs, Z. M.; Hautier, G.; Kanatzidis, M. G.; Snyder, G. J., Thinking Like a Chemist: Intuition in Thermoelectric Materials. *Angew Chem Int Ed Engl* **2016,** *55* (24), 6826-41.
4. Ren, P.; Liu, Y. M.; He, J.; Lv, T.; Gao, J. L.; Xu, G. Y., Recent advances in inorganic material thermoelectrics. *Inorganic Chemistry Frontiers* **2018,** *5* (10), 2380-2398.
5. Snyder, G. J.; Toberer, E. S., Complex thermoelectric materials. *Nature Materials* **2008,** *7* (2), 105-114.
6. Liu, Y.; Cadavid, D.; Ibanez, M.; Ortega, S.; Marti-Sanchez, S.; Dobrozhan, O.; Kovalenko, M. V.; Arbiol, J.; Cabot, A., Thermoelectric properties of semiconductor-metal composites produced by particle blending. *Apl Materials* **2016,** *4* (10), 104813.
7. Rogl, G.; Rogl, P., How nanoparticles can change the figure of merit, ZT, and mechanical properties of skutterudites. *Materials Today Physics* **2017,** *3*, 48-69.
8. Hicks, L. D.; Harman, T. C.; Sun, X.; Dresselhaus, M. S., Experimental study of the effect of quantum-well structures on the thermoelectric figure of merit. *Phys Rev B Condens Matter* **1996,** *53* (16), R10493-R10496.
9. Dean Cheikh, S. K. B., and Bruce S. Dunn, Synthesis and Characterization of Rare-Earth Tellurides and Their Composites For High-Temperature Thermoelectric Applications. In *UCLA Electronic Theses and Dissertations*, 2017.
10. Fleurial, J. P., Thermoelectric Power Generation Materials: Technology and Application Opportunities. *Jom* **2009,** *61* (4), 79-85.
11. Nozariasbmarz, A.; Roy, P.; Zamanipour, Z.; Dycus, J. H.; Cabral, M. J.; LeBeau, J. M.; Krasinski, J. S.; Vashaee, D., Comparison of thermoelectric properties of nanostructured Mg_2Si, $FeSi_2$, SiGe, and nanocomposites of SiGe–Mg_2Si, SiGe–$FeSi_2$. *APL Materials* **2016,** *4* (10), 104814.
12. Ma, J. M. a. K., Richard B., Improving the Mechanical Strength and Power Conversion Efficiency of High Temperature Thermoelectrics. *UCLA.* **2014**.
13. Snyder, G. J., Application of the compatibility factor to the design of segmented and cascaded thermoelectric generators. *Applied Physics Letters* **2004,** *84* (13), 2436-2438.
14. Snyder, G. J.; Ursell, T. S., Thermoelectric efficiency and compatibility. *Phys Rev Lett* **2003,** *91* (14), 148301.
15. Hu, Y.; Wang, J.; Kawamura, A.; Kovnir, K.; Kauzlarich, S. M., $Yb_{14}MgSb_{11}$ and $Ca_{14}MgSb_{11}$—New Mg-Containing Zintl Compounds and Their Structures, Bonding, and Thermoelectric Properties. *Chemistry of Materials* **2014,** *27* (1), 343-351.
16. Cordier, G.; Schafer, H.; Stelter, M., Darstellung und Struktur der Verbindung $Ca_{14}AlSb_{11}$. *Zeitschrift fur anorganische und allgemeine Chemie* **1984,** *519* (12), 183-188.

17. Hu, Y. F.; Cerretti, G.; Wille, E. L. K.; Bux, S. K.; Kauzlarich, S. M., The remarkable crystal chemistry of the $Ca_{14}AlSb_{11}$ structure type, magnetic and thermoelectric properties. *Journal of Solid State Chemistry* **2019,** *271*, 88-102.
18. Cleaves, H. E.; Hiegel, J. M., Properties of high-purity iron. *Journal of Research of the National Bureau of Standards* **1942,** *28* (5), 643-667.
19. Fulkerson, W.; Moore, J. P.; McElroy, D. L., Comparison of the Thermal Conductivity, Electrical Resistivity, and Seebeck Coefficient of a High‐Purity Iron and an Armco Iron to 1000°C. *Journal of Applied Physics* **1966,** *37* (7), 2639-2653.
20. Kunz Wille, E. L.; Grewal, N. S.; Bux, S. K.; Kauzlarich, S. M., Seebeck and Figure of Merit Enhancement by Rare Earth Doping in $Yb_{14-x}RE_xZnSb_{11}$ (x = 0.5). *Materials (Basel)* **2019,** *12* (5), 731.
21. Grebenkemper, J. H.; Klemenz, S.; Albert, B.; Bux, S. K.; Kauzlarich, S. M., Effects of Sc and Y substitution on the structure and thermoelectric properties of $Yb_{14}MnSb_{11}$. *Journal of Solid State Chemistry* **2016,** *242*, 55-61.
22. Grebenkemper, J. H.; Hu, Y. F.; Barrett, D.; Gogna, P.; Huang, C. K.; Bux, S. K.; Kauzlarich, S. M., High Temperature Thermoelectric Properties of $Yb_{14}MnSb_{11}$ Prepared from Reaction of MnSb with the Elements. *Chemistry of Materials* **2015,** *27* (16), 5791-5798.
23. Justl, A. P.; Cerretti, G.; Bux, S. K.; Kauzlarich, S. M., Hydride assisted synthesis of the high temperature thermoelectric phase: Yb14MgSb11. *Journal of Applied Physics* **2019,** *126* (16), 165106.
24. Woo, E. J., Abrasive article comprising a barrier coating. Google Patents: 2001.
25. Kunz Wille, E. L.; Jo, N. H.; Fettinger, J. C.; Canfield, P. C.; Kauzlarich, S. M., Single crystal growth and magnetic properties of the mixed valent Yb containing Zintl phase, $Yb_{14}MgSb_{11}$. *Chem Commun (Camb)* **2018,** *54* (92), 12946-12949.
26. Ohno, S.; Imasato, K.; Anand, S.; Tamaki, H.; Kang, S. D.; Gorai, P.; Sato, H. K.; Toberer, E. S.; Kanno, T.; Snyder, G. J., Phase Boundary Mapping to Obtain n-type Mg_3Sb_2-Based Thermoelectrics. *Joule* **2018,** *2* (1), 141-154.
27. Petříček, V.; Dušek, M.; Palatinus, L., Crystallographic Computing System JANA2006: General features. In *Zeitschrift für Kristallographie - Crystalline Materials*, 2014; Vol. 229, p 345.
28. Rueden, C. T.; Schindelin, J.; Hiner, M. C.; DeZonia, B. E.; Walter, A. E.; Arena, E. T.; Eliceiri, K. W., ImageJ2: ImageJ for the next generation of scientific image data. *BMC Bioinformatics* **2017,** *18* (1), 529.
29. Pike, C. R.; Roberts, A. P.; Verosub, K. L., Characterizing interactions in fine magnetic particle systems using first order reversal curves. *J. Appl. Phys.* **1999,** *85* (9), 6660-6667.
30. Davies, J. E.; Hellwig, O.; Fullerton, E. E.; Denbeaux, G.; Kortright, J. B.; Liu, K., Magnetization reversal of Co/Pt multilayers: Microscopic origin of high-field magnetic irreversibility. *Phys. Rev. B* **2004,** *70* (22), 224434.
31. Winklhofer, M.; Dumas, R. K.; Liu, K., Identifying reversible and irreversible magnetization changes in prototype patterned media using first- and second-order reversal curves. *J. Appl. Phys.* **2008,** *103*, 07C518.
32. Gilbert, D. A.; Zimanyi, G. T.; Dumas, R. K.; Winklhofer, M.; Gomez, A.; Eibagi, N.; Vicent, J. L.; Liu, K., Quantitative Decoding of Interactions in Tunable Nanomagnet Arrays Using First Order Reversal Curves. *Sci. Rep.* **2014,** *4*, 4204.

33. Cho, S. J.; Shahin, A. M.; Long, G. J.; Davies, J. E.; Liu, K.; Grandjean, F.; Kauzlarich, S. M., Magnetic and Mossbauer spectral study of core/shell structured Fe/Au nanoparticles. *Chem. Mater.* **2006,** *18* (4), 960-967.
34. De Toro, J. A.; Vasilakaki, M.; Lee, S. S.; Andersson, M. S.; Normile, P. S.; Yaacoub, N.; Murray, P.; Sánchez, E. H.; Muñiz, P.; Peddis, D.; Mathieu, R.; Liu, K.; Geshev, J.; Trohidou, K. N.; Nogués, J., Remanence Plots as a Probe of Spin Disorder in Magnetic Nanoparticles. *Chem. Mater.* **2017,** *29* (19), 8258-8268.
35. Ravi, V.; Firdosy, S.; Caillat, T.; Lerch, B.; Calamino, A.; Pawlik, R.; Nathal, M.; Sechrist, A.; Buchhalter, J.; Nutt, S., Mechanical Properties of Thermoelectric Skutterudites. *AIP Conference Proceedings* **2008,** *969* (1), 656-662.
36. Ma, J. M.; Firdosy, S. A.; Kaner, R. B.; Fleurial, J.-P.; Ravi, V. A., Hardness and fracture toughness of thermoelectric La3−xTe4. *Journal of Materials Science* **2014,** *49* (3), 1150-1156.
37. Leisure, R. G.; Willis, F. A., Resonant ultrasound spectroscopy. *Journal of Physics-Condensed Matter* **1997,** *9* (28), 6001-6029.
38. Drymiotis, F. R., Resonant Ultrasound Spectroscopy: Overview and Applications. *International Journal of Modern Physics B* **2010,** *24* (9), 1047-1065.
39. Cox, C. A.; Toberer, E. S.; Levchenko, A. A.; Brown, S. R.; Snyder, G. J.; Navrotsky, A.; Kauzlarich, S. M., Structure, Heat Capacity, and High-Temperature Thermal Properties of $Yb_{14}Mn_{1-x}Al_xSb_{11}$. *Chemistry of Materials* **2009,** *21* (7), 1354-1360.
40. Awbery, J. H.; Griffiths, E., The thermal capacity of pure iron. *Proc R Soc Lon Ser-A* **1940,** *174* (A956), 0001-0015.
41. Ravi, V.; Firdosy, S.; Caillat, T.; Brandon, E.; Van der Walde, K.; Maricic, L.; Sayir, A., Thermal Expansion Studies of Selected High-Temperature Thermoelectric Materials. *Journal of Electronic Materials* **2009,** *38* (7), 1433-1442.
42. Kim, H. S.; Gibbs, Z. M.; Tang, Y. L.; Wang, H.; Snyder, G. J., Characterization of Lorenz number with Seebeck coefficient measurement. *Apl Materials* **2015,** *3* (4), 041506.
43. Borup, K. A.; Toberer, E. S.; Zoltan, L. D.; Nakatsukasa, G.; Errico, M.; Fleurial, J. P.; Iversen, B. B.; Snyder, G. J., Measurement of the electrical resistivity and Hall coefficient at high temperatures. *Review of Scientific Instruments* **2012,** *83* (12), 123902.
44. Wood, C.; Zoltan, D.; Stapfer, G., Measurement of Seebeck Coefficient Using a Light-Pulse. *Review of Scientific Instruments* **1985,** *56* (5), 719-722.
45. Brown, S. R.; Kauzlarich, S. M.; Gascoin, F.; Jeffrey Snyder, G., High-temperature thermoelectric studies of $A_{11}Sb_{10}$ (A=Yb, Ca). *Journal of Solid State Chemistry* **2007,** *180* (4), 1414-1420.
46. Makongo, J. P. A.; Darone, G. M.; Xia, S.-Q.; Bobev, S., Non-stoichiometric compositions arising from synergistic electronic and size effects. Synthesis, crystal chemistry and electronic properties of $A_{14}Cd_{1+x}Pn_{11}$ compounds ($0 \leq x \leq 0.3$; A = Sr, Eu; Pn = As, Sb). *Journal of Materials Chemistry C* **2015,** *3* (40), 10388-10400.
47. Cerretti, G.; Villalpando, O.; Fleurial, J. P.; Bux, S. K., Improving electronic properties and mechanical stability of Yb14MnSb11 via W compositing. *Journal of Applied Physics* **2019,** *126* (17), 175102.
48. Kou, X.; Fan, X.; Dumas, R. K.; Lu, Q.; Zhang, Y.; Zhu, H.; Zhang, X.; Liu, K.; Xiao, J. Q., Memory Effect in Magnetic Nanowire Arrays. *Adv. Mater.* **2011,** *23* (11), 1393.
49. Davies, J. E.; Wu, J.; Leighton, C.; Liu, K., Magnetization Reversal and Nanoscopic Magnetic Phase Separation in $La_{1-x}Sr_xCoO_3$. *Phys. Rev. B* **2005,** *72*, 134419.

50. Bhattacharya, S.; Marinescu, D. C.; Morris, J. R.; Sergienko, I. A.; Sales, B.; Mandrus, D.; Keppens, V., Elastic properties of the Zintl ferromagnet $Yb_{14}MnSb_{11}$. *Physical Review B* **2012,** *86* (2), 024402.
51. Gong, L. L.; Wang, Y. H.; Cheng, X. D.; Zhang, R. F.; Zhang, H. P., A novel effective medium theory for modelling the thermal conductivity of porous materials. *International Journal of Heat and Mass Transfer* **2014,** *68*, 295-298.
52. Powell, M. J., Site Percolation in Randomly Packed Spheres. *Physical Review B* **1979,** *20* (10), 4194-4198.
53. Mackey, J.; Dynys, F.; Sehirlioglu, A., Uncertainty analysis for common Seebeck and electrical resistivity measurement systems. *Rev Sci Instrum* **2014,** *85* (8), 085119.
54. Pugh, E. M.; Rostoker, N., Hall Effect in Ferromagnetic Materials. *Reviews of Modern Physics* **1953,** *25* (1), 151-157.
55. Rowe, D. M., Electrical Properties of Hot-Pressed Germanium-Silicon-Boron Alloys. *J Phys D Appl Phys* **1975,** *8* (9), 1092-1103.
56. Fleurial, J.; Borshchevsky, A.; Caillat, T.; Morelli, D. T.; Meisner, G. P. In *High figure of merit in Ce-filled skutterudites*, Fifteenth International Conference on Thermoelectrics. Proceedings ICT '96, 26-29 March 1996; 1996; pp 91-95.

For table of contents only:

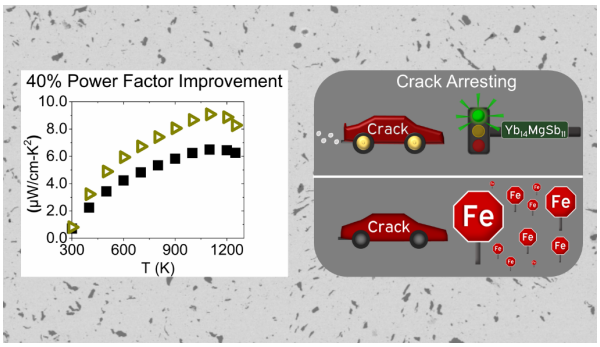

Synopsis:

$Yb_{14}MgSb_{11}$ was synthesized via a fast, scalable mechanical milling to spark plasma sintering synthesis. Scanning electron microscopy, transition electron microscopy, powder X-ray diffraction, and first-order reversal curves were used to probe sample purity and show that Fe does not diffuse or substitute into the $Yb_{14}MgSb_{11}$ structure. Resonant ultrasound spectroscopy measurements show the 8 volume % composite has stiffened and Fe inclusions have shown to arrest cracks. High temperature thermoelectric measurements show the zT of the 3 volume % Fe composite has improved by 11% over pristine $Yb_{14}MgSb_{11}$ and the power factor of the 8 volume % Fe composite has improved by 40%.